Materials Research. 2022; 25:e20210383
DOI: https://doi.org/10.1590/1980-5373-MR-2021-0383

Interfacial Bonding Strength in Cement Mortar Beams Reinforced with Metamaterial Bars

C. Q. Ramírez[a,c], *C. V. S. Santos*[b], *P. C. Gonçalves*[b,c], *M. V. Gelfuso*[b,d]*, *V. C. Santos*[b], *J. A. G. Sánchez*[b,c]

[a]*Universidade de São Paulo, Escola de Engenharia de São Carlos, Departamento de Engenharia de Estruturas, Av. Trabalhador São-carlense, 400, São Carlos SP, Brasil.*
[b]*Universidade Federal de Itajubá, Av. BPS, 1303, Itajubá, MG, Brasil.*
[c]*Universidade Federal de Itajubá, Metamaterial and Structures Unifei (MSU), Itajubá, MG, Brasil.*
[d]*Universidade Federal de Itajubá, Grupo de Desenvolvimento de Materiais Funcionais (GDMaF), Itajubá, MG, Brasil.*

Received: July 25, 2021; Revised: April 10, 2022; Accepted: April 11, 2022

Reinforced concrete beam (RCB) elements show low mechanical performance when interfacial bonding strength (IBS) is not well controlled. New tailorable material-structure arrangements - Metamaterials - offer solutions to the IBS problem. This paper analyzes the mechanical characteristics of IBS on RCBs for reinforced cement mortar containing Metamaterial bars (MMB) that were machined from SAE 1020 Carbon steel. Each MMB has a stepped geometrical shape, with a cylindrical bar divided into equal-length segments, along with a 'rise height' (p) change. Four geometries were defined, i.e., *R0*− Smooth bar, *R1*− p = 0.1mm, *R2*− p =0.3mm and *R3*− p=0.5mm. Three-point flexural strength tests were performed on the RCBs to determine the maximum bond strength (ML) between the MMB and cement mortar. Images of interfacial regions were obtained using SEM and 3D Roughness Reconstruction software to calculate the average roughness (*Ra*) and the roughness height (*Rz*). The reinforcement MMB geometry had a significant impact on the ML results, particularly on the first crack strength and the failure mode. The *R3* geometry ML values were higher than the other tested geometries (44.5%). The results of the scale models are encouraging and offer a novel and prospective direction for further experimental and even numerical Metamaterial research to improve interfacial bond strength.

Keywords: *Interfacial bonding strength, metamaterial, concrete.*

1. Introduction

Metamaterials are artificially structured materials with mechanical and physical properties that generally counterintuitive. They are often purposefully tailored to achieve specific target design goals. Metamaterials have been defined by Bertoldi et al.[1], as periodically arranged building blocks that exhibit properties and functionalities superior than those conceived solely by their constituent materials (or combinations between them).

Recent advances in manufacturing technologies, e.g., fused deposition modelling; selective laser synthesize; two-photon lithography; 3D printed patterns for metal casting; amongst others - have led to real-world implementations for Metamaterials in a number/variety of engineering fields. However, most research has focused on physics[2,3] and mechanical engineering applications[1,4-6]. For this reason, civil engineering applications remain open to question/investigations, and therefore warrant closer examination.

Most literature on Metamaterials applied to civil-engineering has been limited to three main research topics, i.e., mechanical vibration damping[7,8], printing concrete[9,10] and seismic shields[11,12]. Very few studies have investigated Metamaterials for reinforced concrete. Farina et al.[13] and Farina et al.[14], pioneered a study that used rebars with surfaces designed using Metamaterials to improve the mechanical performance.

The proposed Metamaterial bar geometry seeks to improve the strength of reinforced concrete via geometric manipulation, while also proposing Metamaterials that can be feasibly manufactured.

1.1. Metamaterials in reinforced concrete

Some studies have examined using Metamaterial structures in anchors[15,16], composite structures, and reinforced concrete. Research on reinforced concrete seeks to offer improvements to composite structure strength via improved roughness or chemical adherence, or by adding ribs[17-19]. Other studies are also being carried out on Metamaterial structures for sandwich panels[20], or by modifying the concrete matrix[21].

Some research in reinforced concrete[13,14,22] has studied using rebars with Metamaterial surface designs to improve mechanical performance. The authors developed high energy absorption capacity designs by increasing the interfacial bonding strength (mortar-reinforcement), and designing reinforcement surface roughness with additive manufacturing

*e-mail: mvgelfuso@unifei.edu.br

technique. Farina et al.[13,14] analyzed the effect of geometrical shapes on surface roughness, and proposed a variety of superficial geometries for both polymeric and metallic bars. It is worth noting that[13,14], flexural tests, and microscopic characterization of fiber surfaces, were performed after the beams were tested and broken, in both studies.

As cited in literature[23,24], there have been no conclusive studies on Metamaterial designs for use as concrete reinforcements with non-linear characteristics. Literature shows that it is possible to interfere with or improve the reinforced concrete or composite structures strength by using Metamaterials. However, to the extent of the our literature review, there are no studies testing using Metamaterials to construct the geometry of reinforcing bars.

1.2. Reinforcing concrete iteration: bond

From the beginning of the twentieth century, conventional rib rebars have increased interfacial bond strength[25]. Stress distribution was first analyzed by Watstein[26,27], and steel bar and concrete slip resistance was studied via bending tests[28].

Several studies have shown that there are different factors that influence the steel–concrete interface[27]. Particularly, Angst et al.[29], showed that some factors can significantly influence RC structural and durability performance.

The reinforcing-to-concrete bond allows longitudinal forces to be transferred from the bar to the surrounding concrete. This interaction is analyzed via the bond strength, Maximum Load (ML), and when this is not a good factor the weakest structure point can be used[27]. Bonding performance for conventional steel ribs rebar can be obtained by appropriately combining height and rib spacing (s_R), and bar diameter (d_b) using the "bond index" f_R or "relative rib area"[1] ($f_R = A_R/(\pi d_b s_R)$)[27]. In general, higher bond strengths can be defined by increasing the rib diameter (increasing area). In order to study the bond for reinforcing concrete without ribs, we have proposed a new geometry for the rebar; naturally increasing the concrete volume between geometrical parts, to improve the "bond index" consequently leading to better performance.

Reinforcing-to-concrete interaction is determined via the bonding strength. It is well known that this is poorly controlled, as RC elements have low mechanical performance. Traditionally, bonding strength is controlled by the using long steel reinforcing bars with a ribbed surfaces.

According to Tepfers et al.[27], several technological aspects come into play for interfacial bonding strength, e.g., concrete cover, clear space between the bars, number of bar layers and bundled bars, casting direction with respect to the bar orientation, bar placement with respect to the free fluid concrete surface, the roughness surface, chemical adhesion, and micromechanical interaction. The authors also reported on other less intuitive parameters, e.g., the Poisson ratio, the bar size or loading-time history, among others. However, most studies were conducted for the roughness surface and chemical adhesion areas. To the best our knowledge, there have been no studies in the field on tailored Metamaterial cells for increased (or improved) bonding strength.

[1] AR is the area of the projection of a single rib.

Further information on interface strength between concrete and different kinds of reinforcements can be found in studies by Chang et al.[30], Nematzadeh and Ghadami[31], Rahdar and Ghalehnovi[32], Dai et al.[33], Kwak and Kim[34] and Chang et al.[30], among others.

This paper proposes improving the interfacial bonding between mortar and reinforcement by employing a novel reinforcement geometry, which is known to benefit from the horizontal directions of the bending normal stresses. Our proposed Metamaterial cell is a cylindrical stepped bar divided into N segments of constant cross-section of equal length, with alternating peak diameters located lengthwise at every distance "d", as shown in Figure 1.

More specifically, this proposed geometrical configuration provides a direct restriction of the normal bending stress as a result of the increased contact area (especially if compared to a uniform cross-section bar). This particular feature results in improved bonding strength, given the effects of the whole Metamaterial shape, rather than just surface roughness control.

2. Experimental Procedure

In this study, the interfacial bonding between the mortar and reinforcement was analyzed using three-point flexural strength tests (or the three-point bending flexural test), based on ASTM C1018[35] to calculate the flexural strength and the average rupture modulus , under displacement control (with a rate of 0.5 mm/s) according to Farina et al.[13]. It is important to note that Farina et al.[13] and Farina et al.[14], are among the few who have explored the effects of geometrical shapes on surface roughness, using superficial geometries for both polymeric and metallic bars in interfacial bonding strength. Thus, to compare our results with data from literature, we have used the same methodology based on ASTM C1018[35] to calculate flexural strength and the average rupture modulus.

The bending strength tests were carried out primarily to determine: (a) the maximum bond strength (ML) between

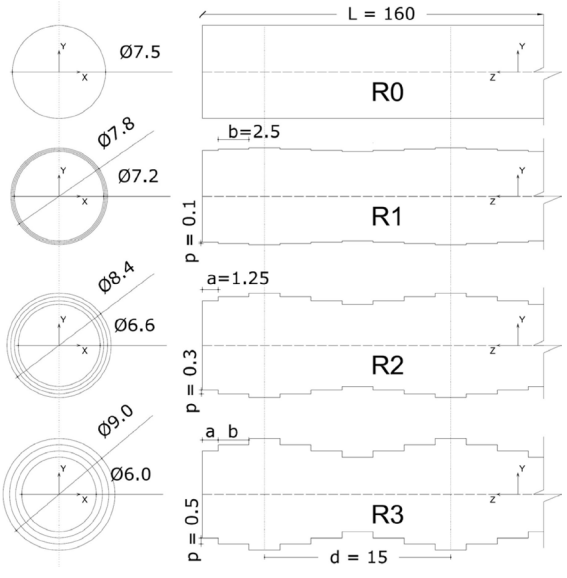

Figure 1. Illustration of Metamaterial reinforcement bars: cross section XY and YZ section.

the Metamaterial bars (Carbon steel SAE 1020) and the cement mortar; (b) the first crack strength; and (c) the fracture toughness. It is worth mentioning that all prismatic mortar beams (sizes 40 mm x 40 mm x 160 mm) were fabricated with a target compressive strength of 8 MPa[13].

The specimens were reinforced with four different types of bars, each 160 mm in length (L). Each reinforcement cell features a stepped geometrical shape, i.e. a cylindrical bar divided into equal-length segments of constant area, with a horizontal distance at 15 mm between alternating peaks of the two designed cells, which was repeated for all bars; The 'tread depth' was constant (b = 2.5 mm), and the 'rise height' (p) change. Four kinds of geometries are defined: *R0*− Smooth bar, *R1*− p = 0.1 mm, *R2*− p = 0.3 mm and *R3*− p = 0.5 mm. These are shown in Figure 1.

Furthermore, the microstructural morphology aspect of the reinforcement surface was analyzed using a Scanning Electronic Microscopy (SEM) to examine the mortar adhered to the reinforcement. The SEM image placement was previously selected by optical images. The optical camera was activated, and the image was displayed on a main viewing window screen. Then, the sample that would be magnified on the main viewing window (SEM images) was displayed on the optical overview window. Three-dimensional images (3D images) and sub-micrometer roughness measurements were generated using the 3D Roughness Reconstruction software (Phenom PRO-X). The average roughness (*Ra*), and the roughness height (*Rz*) were calculated using the software's built-in features.

Twelve metallic bars, three for each model *R0*, *R1*, *R2* e *R3* (Figure 1) were manufactured using a classical lathe turning process (refer to Figure 2), since this technique allows for a more practical and industrial approach. It is also worth mentioning that the reinforced material volume of all the specimens was kept constant.

Figure 2. Photographs of 3D Metamaterial reinforcement bars.

2.1. Limitations

The experimental results reported herein should be considered in the light of some limitations/caveats:

- Concrete beams weren't used, and all prismatic mortar beams were fabricated as a reduced-scale models, with a target compressive strength at 8 MPa, as per Farina et al.[13];
- The interfacial bonding between the mortar and reinforcement was analyzed using three-point flexural strength tests based on ASTM C1018, as per Farina et al.[13], with a limited number of tests;
- It is also worth mentioning that the reinforced material volume for all the specimens remained constant; and
- Variations in roughness from manufacturing were not considered.

3. Results and Discussions

Typical Failures-Flexure are shown in Figure 3a and the failure modes of the tested reinforced beams, *R1* − 1, *R2* − 1 e *R3* − 1, are shown in Figure 3b to 3d. Failure processes with synchronized picture and video for the load-deflection curve for *R0* − 1, *R1* − 3, *R2* – 2, and *R3* − 2, are shown in Figure 4.

The *R0* beams showed flexural crack debonding in the region where bending moment reached its maximum, and the principal tension exceeds the material's tensile strength[36], which is typically characteristic of beams with low-reinforcement ratios. By contrast, beams *R1* and *R2* show shear-type mixed-mode failures, combined tension and shear stresses, whit cracks propagating approximately perpendicularly to the principal stresses regions, where the shear-loading is negligible[36]. Beams *R3* showed a shear-type failure, with a diagonal crack propagating from the boundary to the application point of the vertical load. Detailed information on the influence of the bonding strength on failure modes can be found in Kotsovou and Kotsovos[37].

3.1. Maximum Load (ML)

In this study, we considered that the ML is reached just before crack onset[13]. Referring back to Figure 5, one can see that the unreinforced beam withheld a ML at roughly 900 N. One can also see that the ML for the *R0* geometry ranged from 1600 N to 2700 N, while these values ranged from 2000 N to 2400 N for the *R1* configuration. Similarly, the *R2* geometry showed a ML range at 2100 N < ML(*R2*) < 2600 N, while this range was 3100 N < ML(*R3*) < 3200 N for *R3*. In summary, the average ML for each configuration was 2148.07 N for *R0*, 2145.57 N for *R1*, 2374.1 N for *R2* and 3107.23 N for *R3*, respectively, as shown in Table 1.

The results in Table 1 show that, contrary to what was expected, the ML for reinforced beams with *R1* and *R2* geometries did not improve significantly compared to *R0*. However, this may be due to the high standard deviation (SD) with the *R0* geometry, although the *R3* geometry ML value was higher than the results of the other tested geometries. Considering the lower ML value for each

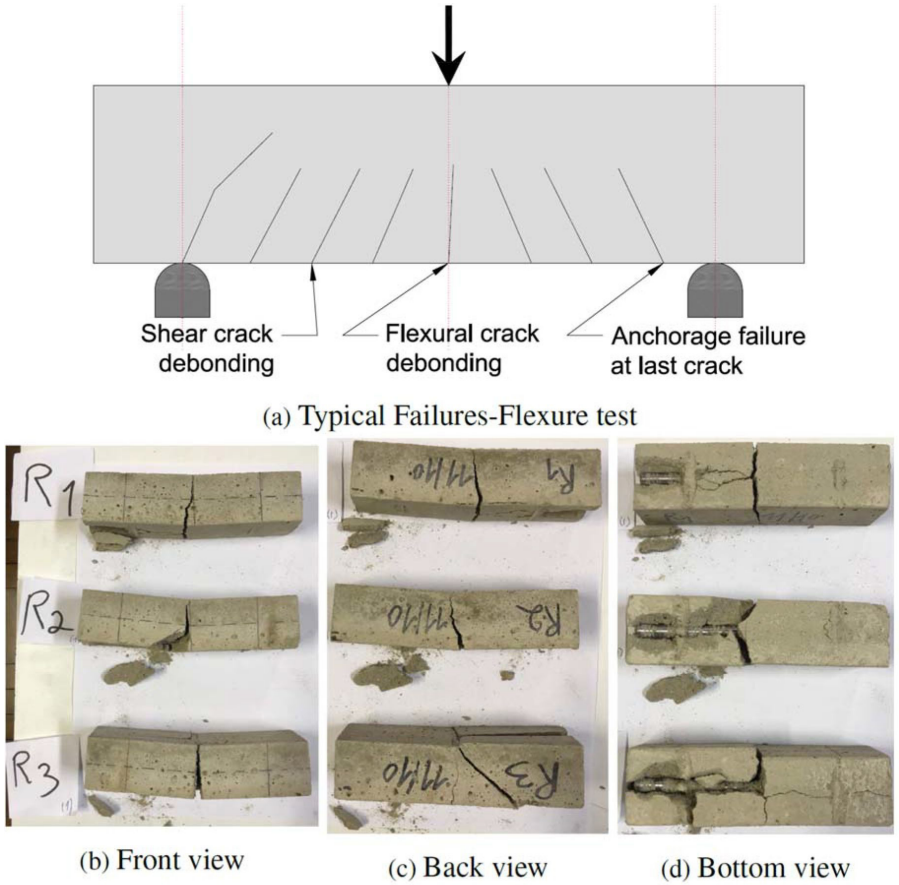

Figure 3. Typical failures-flexure and results for R1-1, R2-1 e R3-1.

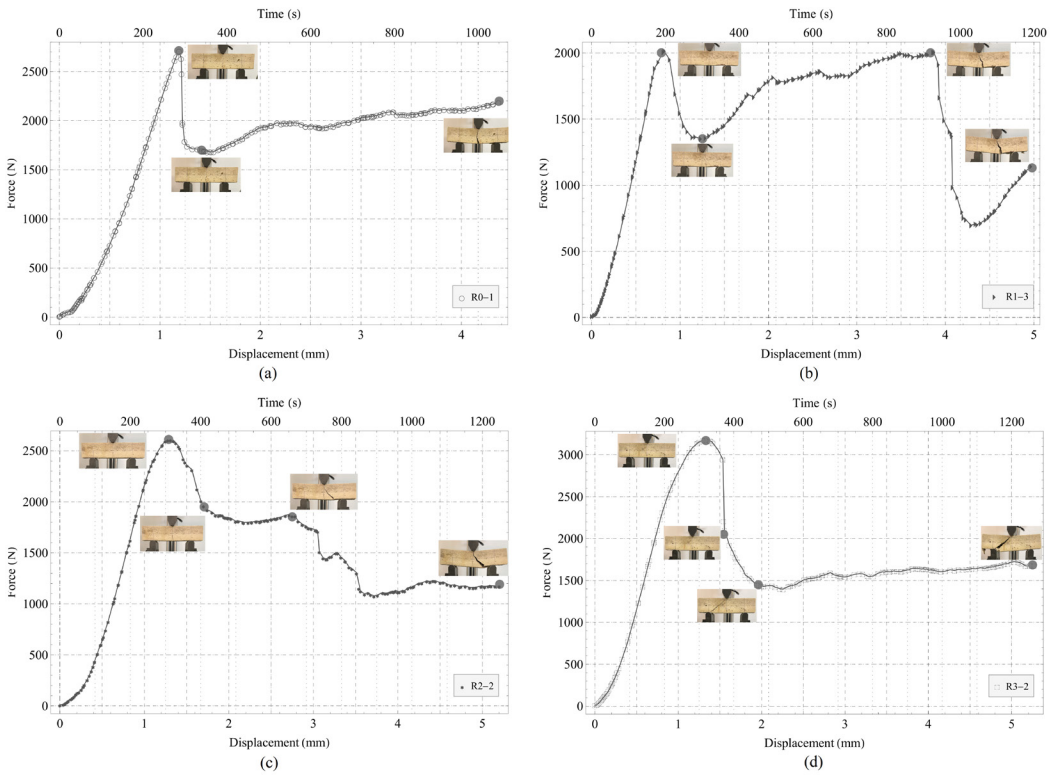

Figure 4. Synchronization between pictures of video and load-deflection (or vertical displacement) curve.

geometry, to compare the carrying capacity before crack onsets, we noted that the ML with *R3* was approximately twice the ML with *R0*.

The Load-deflection curves of all the specimens with different reinforcement geometries (including the unreinforced beam) are shown in Figure 5, detailing the applied force (vertical axis) versus the mid-span deflection (bottom horizontal axis) and the loading time (top horizontal axis).

Analyzing the failure mode shown in Figure 5, one can see that the unreinforced beam collapsed quickly after crack onset. By contrast, this was not observed for the reinforced bars. For the *R0* geometry, all curves exhibited widely varying behavior. The *R0* − 1 specimen showed a sudden drop in the carrying capacity, immediately after the crack onset, followed by a hardening interval with an almost constant slope. The *R0* − 2 showed a load drop after the crack onset, a wide hardening interval with a moderate slope; and a softening branch before failure. The *R0* − 3 showed a small hardening branch, and a quick load drop before failure.

All curves for *R0* specimens showed a marked load drops after crack onset. The *R1* and *R2* curves showed a drop in carrying capacity after crack onset, followed by a hardening branch with smoother slopes, a second load drop and a softening branch before the failure. Reinforced beams with the *R3* geometry showed a load drop after crack onset, and a hardening branch with a slight slope. This leads us to conclude that the slope of curves after crack onset, for *R1*, *R2* and *R3* geometries, were smoother than the curves for *R0* specimens.

3.2. First crack strength

We took approximate first peak in the Load-deflection curve to define and locate the first crack in the tests. The average rupture modulus[35] was also taken into account in this study, as shown in Figure 6, to calculate the flexural strength.

According to Figure 3d, because most fractures occurred on the tension surface, within the middle-third of the span length, we calculated the rupture modulus using the following expression: $R = PL/(bd^2)$ as per Test Method C− 78; where P = maximum applied load, L = span length, b = average width and d = average depth of specimen at the fracture. Using this data, we inferred that R_{R0}, R_{R1} and R_{R2} resulted in no significant differences, while R_{R3} had the highest value (44.5%).

Table 1. Left - ML: Average of Maximum Load and SD: Standard Deviation. Right - ML for each test.

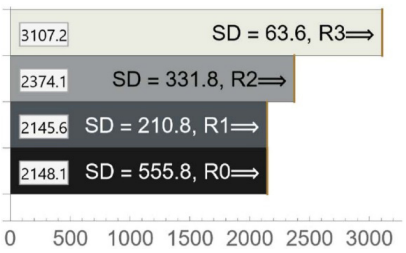

ML (N)		
3048.6	3174.9	3098.2
2139.5	2608.7	
2032.1	2388.9	2015.9
2709.4	1597.9	2136.9

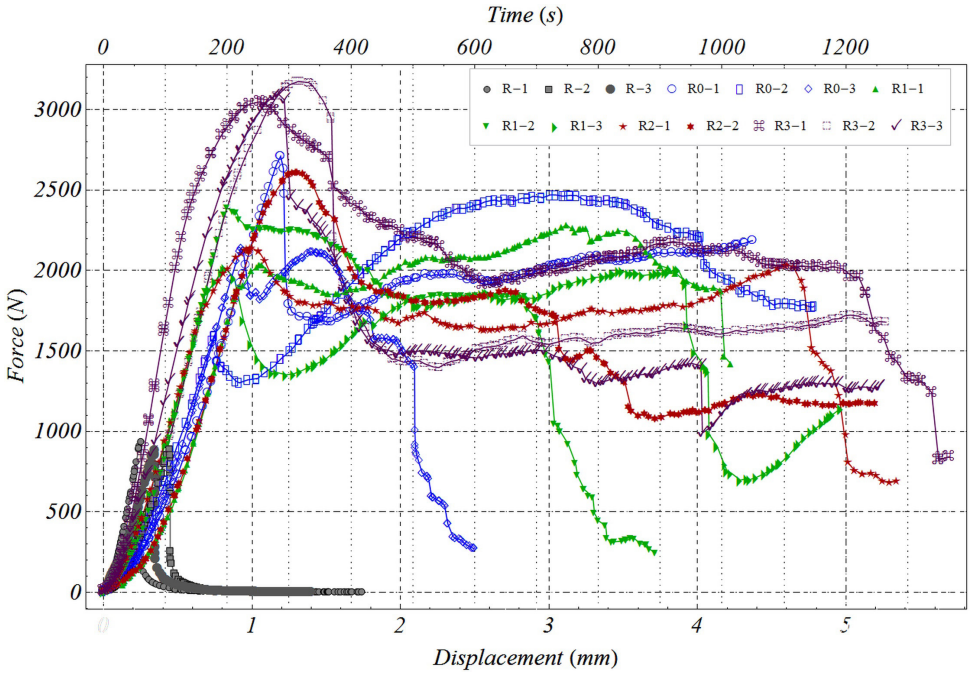

Figure 5. Force vs. vertical displacement (or load-deflection) curves of all the specimens.

3.3. Fracture toughness

The ASTM C1018[35] specifications were adapted for the materials used in this study. Then, the energy absorption capacity for the reinforcements beams was obtained via: I = A(δ = 3δ)/A(δ), where A(δ) denoting the area under the load-deflection, from the origin, up to the mid-span deflection (δ), which corresponds to the first crack load of the specimen, while A(δ = 3δ) represents the area under the curve, which corresponds to 3δ.

Figure 7 gives a measure of the relative energy absorption capacity for each reinforcement beam, while Figure 6 (b) gives the mean values for specimens for each morphology surface group (*R0, R1, R2, R3*).

Disregarding the discrepant value of specimen $R0-2$, it is worth noting that most of the average values for energy absorption capacity, represented by index I, showed gradual reductions as the step height grew, as showed in Figure 5. The results also indicate that *R3* beams had smooth behavior after the first crack, up until rupture (Figure 5), presumably indicating better bond strength.

The results from Figure 8, 9, and 10 show that reinforced specimens have increased energy absorption capacity compared

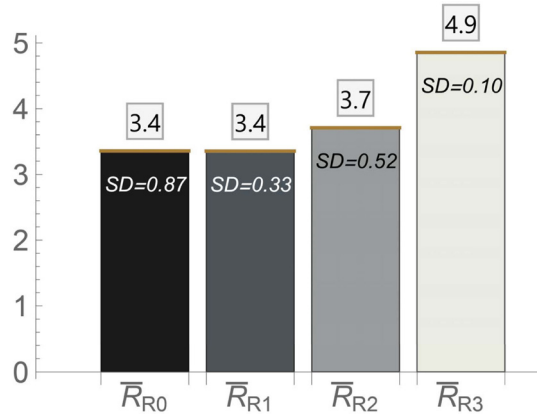

Figure 6. Modulus of rupture, $\underline{R}_{med}$.

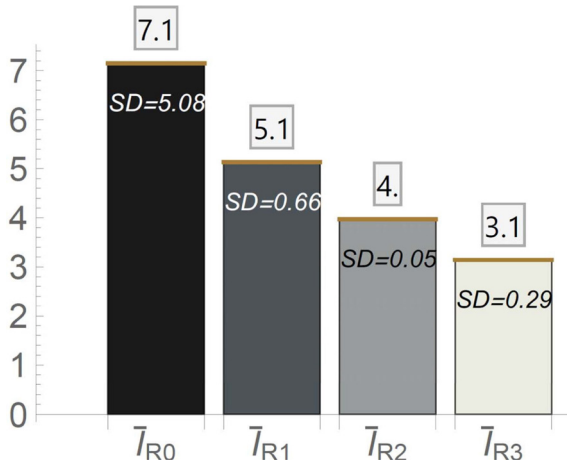

Figure 7. Measure of the relative energy absorption capacity of Reinforced beam, I_m (without I_{R0-2}).

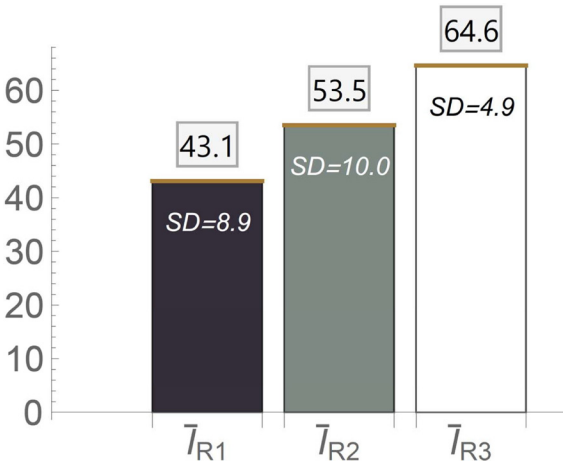

Figure 8. Measure of the relative energy absorption capacity of Reinforced beam against the unreinforced one, $\underline{I} = \frac{A(3\delta)}{A_R(\delta)}$.

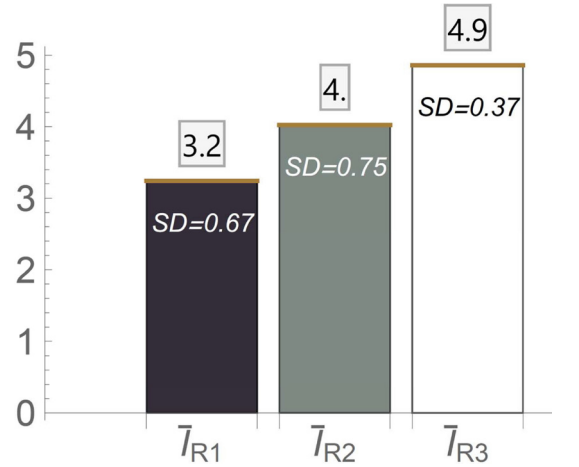

Figure 9. Measure of the relative energy absorption capacity of reinforced beam against the R0, $\underline{I} = \frac{A(3\delta)}{A_{R0}(\delta)}$.

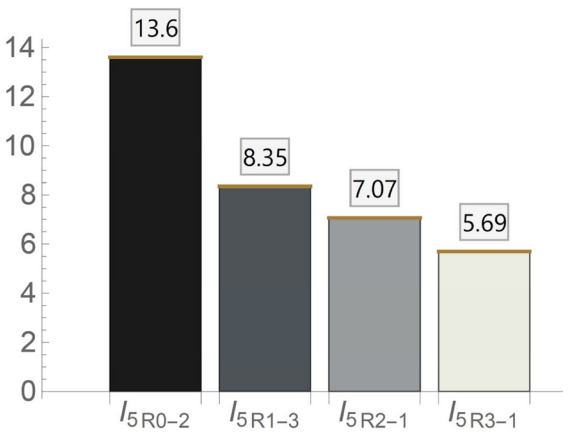

Figure 10. Measure of the relative energy absorption capacity of reinforced beam, $\underline{I}_5 = \frac{A(5\delta)}{A(\delta)}$.

to unreinforced specimens. One can see that the reinforced beams *R3* exhibited larger toughness values compared to the other reinforced mortar beams. This is shown in Figure 5, where the reinforced beams *R3*, *R2* and *R1* were benchmarked against the smooth reinforced beam (*R0*). The reinforced beams examined in this study showed high toughness and residual resistance in the first post-crack regime, followed by brittle behavior for large deformations. However, most reinforced specimens showed flexural collapse after 5δ, resulting in more deflection.

3.4. Surface microscopy analyzes of meta-reinforcement

Figure 11 gives the nomenclature for the microstructural images of the observed areas using the SEM technique. Regions A, B, C and D define the steps, the regions AB, BC and BD area between steps.

Figure 12, 13 and 14 show micrographic images and the 3D roughness reconstructions for the *R1*, *R2* and *R3* specimens. Regions A, B, C and D (defined as steps) were almost free of mortar, for specimens *R1* (Figure 12a and 12b) and *R2* (Figure 13a and 13b), while regions AB, BC and BD (representing areas between the steps) showed a slight mortar accumulations. A significant difference was observed for the specimen *R3* (Figure 14a and 14b). When comparing *R1* and *R2*, the optical and SEM images showed that *R3* surface had the most mortar buildup. The SEM characterization for the *R3* morphology showed that the built size of the macroscopic reliefs of these specimens caused notable mortar anchorage, especially on CD regions, promoted by larger contact areas. The images from the 3D roughness reconstructions for all the specimens (12, 13 and 14), give lines traced to obtain *Rz* and *Ra* values (Table 2). The *Ra* and *Rz* values were obtained from 3 lines traced on surfaces of the metallic bars (*R1*, *R2* and *R3*) at the very instant that the SEM images were observed.

The modest increase of *Rz* for *R1* specimens is related to the fact that this bar has very smooth steps, which were insufficient for anchoring mortar, but there was enough roughness to be detected by *Rz* analyzes. No relevant change was observed to the *Ra* or *Rz* parameters for *R2* and *R3* bars. The steps were sufficiently filled with mortar to leave the bar surfaces relatively plane in both cases.

However, the *Ra* and *Rz* values cannot be used to explain the high mechanical strength observed for specimen *R3* (Figure 15). Nevertheless, SEM images show a significant buildup of mortar, resulting from the *R3* geometry. This effect can be attributed to the role played by the vertical reinforcement step, which is directly opposed to the normal mortar stress, stopping mortar slippage, resulting in improved anchorage between Metamaterial reinforcement bars on the matrix interface.

4. Summary and Conclusions

In this study, we experimentally investigated and analyzed the interfacial bonding force, between mortar and reinforcement in RC beams, given the need to extend the state-of-the-art on Metamaterials applied to civil-engineering.

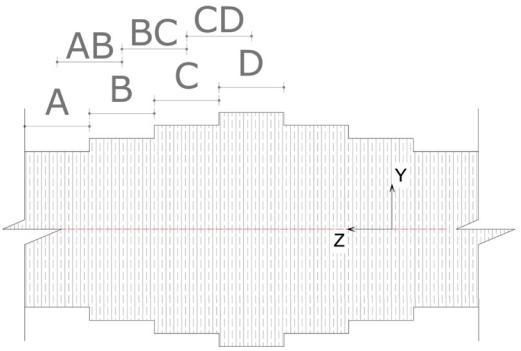

Figure 11. Nomenclature used to define the different parts of the meta-reinforcement surface.

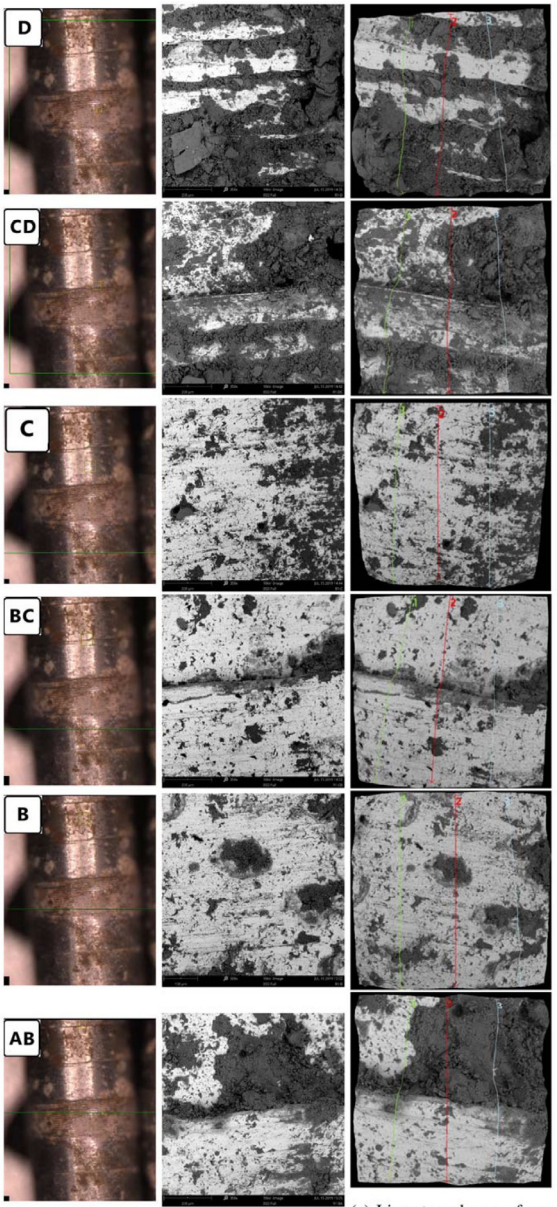

(a) Optical Images (b) SEM images, 350*x* (c) Lines traced on surfaces to obtain R_z and R_a values, 350*x*

Figure 12. 3D roughness reconstruction of R1.

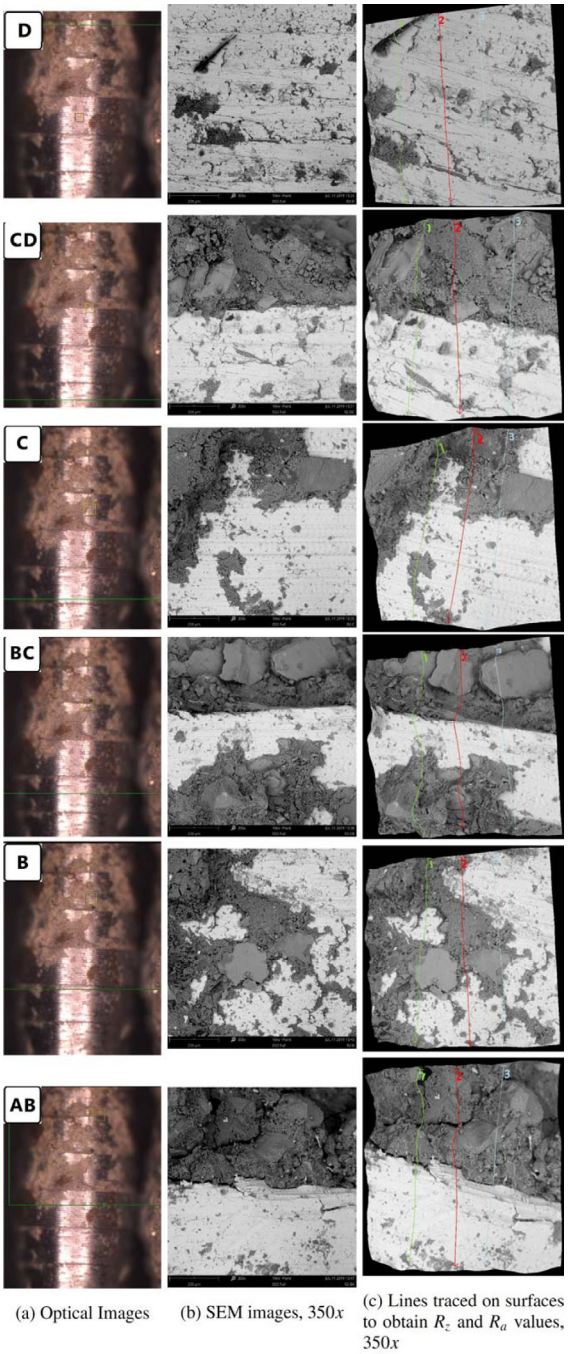

(a) Optical Images (b) SEM images, 350*x* (c) Lines traced on surfaces to obtain R_z and R_a values, 350*x*

Figure 13. 3D roughness reconstruction of R2.

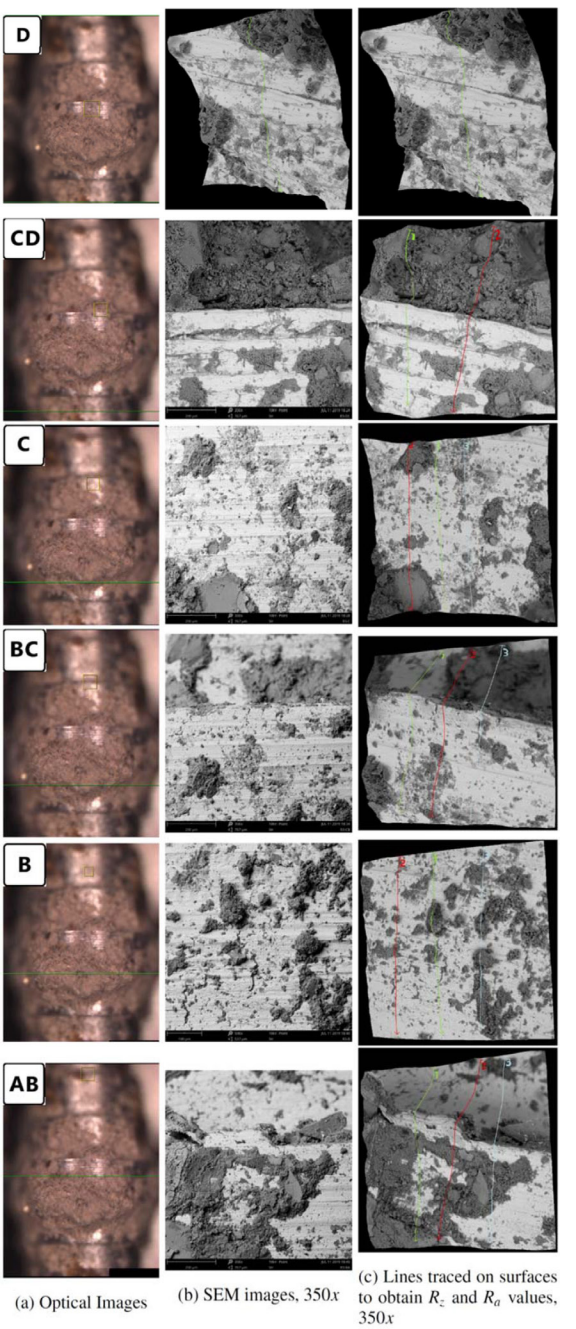

(a) Optical Images (b) SEM images, 350*x* (c) Lines traced on surfaces to obtain R_z and R_a values, 350*x*

Figure 14. 3D roughness reconstruction of R3.

Table 2. Average roughness (*Ra*) and the roughness height (*Rz*) in surfaces defined in Figure 11.

Surface	*Rz* (μm)			*Ra* (μm)		
	R1	*R2*	*R3*	*R1*	*R2*	*R3*
A	7.74	6.73	4.66	1.22	1.00	0.50
AB	7.63	5.72	7.74	1.23	0.94	1.15
B	8.02	6.99	8.37	1.20	0.96	1.30
BC	6.69	6.72	6.80	0.98	1.05	0.82
C	7.60	6.38	7.12	1.16	0.96	0.95
CD	9.23	7.29	7.44	1.67	1.09	1.10
D	9.10	6.47	8.80	1.56	0.75	1.38

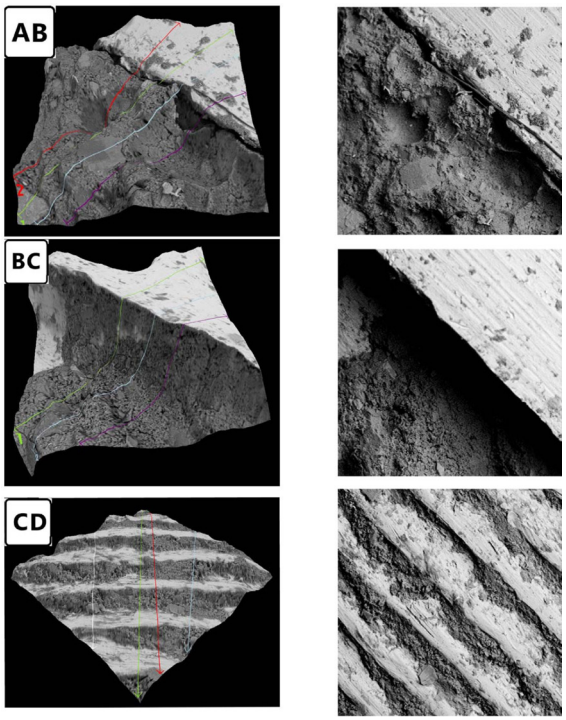

Figure 15. Surface morphology, isometric view for regions: AB, BC and CD of R3.

This study sought to improve the interfacial bonding strength for reinforced concrete by controlling rebar geometries using the Metamaterial concept.

The classical lathe turning process was used to manufacture metallic bars, since it is practical and efficient, considering the geometry studied, and the scale models.

The proposed Metamaterial geometry acts as an obstacle to compression in flexural tests.

The beams showed improved performance for maximum load and rupture modulus as the 'rise height' increased.

The average ML value was significantly higher in bars reinforced with *R3* geometry compared to *R0*, *R1* and *R2* geometries. The relative increase of ML to *R3* was about 44.5%, relative to *R0*. This indicates that ML was strongly influenced by the geometry, and that the *R3* geometry tends to increase the interfacial bonding force.

The curve slopes were smoother (applied force vs. mid-span deflection) after crack onset for geometries *R1*, *R2* and *R3*, than for *R0* geometries, which had a steeper slope (sudden drop) after crack onset. Furthermore, the failure modes for beams with different reinforcement geometries indicate a transition in crack patterns, from flexural failure mode for *R0* specimens, through a shear failure mixed-mode for the *R1* and *R2* beams, to a shear failure mode for *R3*, suggesting that the geometry used as reinforcement in RC beams, and its scale, can strongly influence interfacial bonding.

The *Ra* and *Rz* parameters did not provide significant information for understanding increases to mechanical strength observed for *R3* specimens. However, the SEM images showed mortar buildups constrained by the vertical step in the reinforcement bars, which are directly opposed to the normal mortar stress, preventing slipping between the mortar and reinforcement.

Given the importance of improving interfacial bonding strength, the results presented in this paper using Metamaterials are encouraging, and offer a novel prospective direction for using RC beam top reinforcements. More research and innovation are needed to improve interfacial bonding strength via Metamaterials. Further experimental and numerical models should be the subject of future research, to analyze the geometrical parameters and their influence on the interfacial bonding strength.

5. Acknowledgments

This study was supported by Minas Gerais State Agency for Research and Development (FAPEMIG), ANP (National Agency of Petroleum, Natural Gas and Biofuels of Brazil) and Shell Brazil, via the Clause Investment in Research, Development, and Innovation, contained in contracts for Exploration, Development, and Production of Oil and Natural Gas. The authors thanks to CNPq (National Council for Scientific and Technological Development of Brazil), proc. 439088/2018-6 - MCTIC/CNPQ No 28/2018 Universal Faixa A, and for the Research Productivity Grant (Proc.:312640/2017-0).

6. References

1. Bertoldi K, Vitelli V, Christensen J, Van Hecke M. Flexible mechanical metamaterials. Nat Rev Mater. 2017;2(11):17066.
2. Schurig D, Mock JJ, Justice BJ, Cummer SA, Pendry JB, Starr AF, et al. Metamaterial electromagnetic cloak at microwave frequencies. Science. 2006;314(5801):977-80.
3. Meinzer N, Barnes WL, Hooper IR. Plasmonic meta-atoms and metasurfaces. Nat Photonics. 2014;8(12):889-98.
4. Tong XC. Functional metamaterials and metadevices. Cham: Springer International Publishing; 2018. Vol. 262.
5. Berger JB, Wadley HNG, McMeeking RM. Mechanical metamaterials at the theoretical limit of isotropic elastic stiffness. Nature. 2017;543(7646):533-7.
6. Yu X, Zhou J, Liang H, Jiang Z, Wu L. Mechanical metamaterials associated with stiffness, rigidity and compressibility: a brief review. Prog Mater Sci. 2018;94:114-73.
7. Pai PF. Metamaterial-based broadband elastic wave absorber. J Intell Mater Syst Struct. 2010;21(5):517-28.
8. Mitchell SJ, Pandolfi A, Ortiz M. Metaconcrete: designed aggregates to enhance dynamic performance. J Mech Phys Solids. 2014;65(1):69-81.
9. Buswell RA, Leal de Silva WR, Jones SZ, Dirrenberger J. 3D printing using concrete extrusion: a roadmap for research. Cement Concr Res. 2018;112(May):37-49.
10. Feng P, Meng X, Zhang H. Mechanical behavior of FRP sheets reinforced 3D elements printed with cementitious materials. Compos Struct. 2015;134:331-42.
11. Yan Y, Laskar A, Cheng Z, Menq F, Tang Y, Mo YL, et al. Seismic isolation of two dimensional periodic foundations. J Appl Phys. 2014;116(4):044908.
12. Palermo A, Krödel S, Marzani A, Daraio C. Engineered metabarrier as shield from seismic surface waves. Sci Rep. 2016;6(1):39356.
13. Farina I, Fabbrocino F, Carpentieri G, Modano M, Amendola A, Goodall R. On the reinforcement of cement mortars through 3D printed polymeric and metallic fi bers. Compos Part B. 2015;90:76-85.

14. Farina I, Fabbrocino F, Colangelo F, Feo L, Fraternali F. Surface roughness effects on the reinforcement of cement mortars through 3D printed metallic fibers. Compos, Part B Eng. 2016;99:305-11.
15. Ren X, Das R, Tran P, Ngo TD, Xie YM. Auxetic metamaterials and structures: a review. Smart Mater Struct. 2018;27(2)
16. Ren X, Shen J, Tran P, Ngo TD, Xie YM. Auxetic nail: design and experimental study. Compos Struct. 2018;184:288-98.
17. Tran MT, Vu XH, Ferrier E. Experimental and numerical investigation of carbon textile/cementitious matrix interfacebehaviourfrom pull-out tests. Constr Build Mater. 2021;282:122634.
18. Miranda MP, Morsch IB, Brisotto DS, Bittencourt E, Carvalho EP. Steel-concrete bond behavior: an experimental and numerical study. Constr Build Mater. 2021;271:121918.
19. De Maio U, Fabbrocino F, Greco F, Leonetti L, Lonetti P. A study of concrete cover separation failure in FRP-plated RC beams via an inter-element fracture approach. Compos Struct. 2019;212(January):625-36.
20. Hou S, Li T, Jia Z, Wang L. Mechanical properties of sandwich composites with 3d-printed auxetic and non-auxetic lattice cores under low velocity impact. Mater Des. 2018;160:1305-21.
21. Zhong R, Ren X, Yu Zhang X, Luo C, Zhang Y, Min Xie Y. Mechanical properties of concrete composites with auxetic single and layered honeycomb structures. Constr Build Mater. 2022;322:126453.
22. Fabbrocino F, Farina I, Amendola A, Feo L, Fraternali F. Optimal design and additive manufacturing of novel reinforcing elements for composite materials. In 7th European congress on computational methods in applied sciences and engineering; Crete, Greece. Proceedings. Athens: Institute of Structural Analysis and Antiseismic Research; 2016. p. 1893-908.
23. Li T, Hu X, Chen Y, Wang L. Harnessing out-of-plane deformation to design 3D architected lattice metamaterials with tunable Poisson's ratio. Sci Rep. 2017;7(1):1-10.
24. Zhang G, Khandelwal K. Computational design of finite strain auxetic metamaterials via topology optimization and nonlinear homogenization. Comput Methods Appl Mech Eng. 2019;356:490-527.
25. Abrams DA. Test of bond between concrete and steel. Urbana: University of Illions; 1913.
26. Watstein D. Bond stress in concrete pull-out specimens. ACI J. 1941;38:37-50.
27. Tepfers R, Achillides Z, Azizinamini A, Balázs G, Vliet AB, Cabrera J, et al. Bond of reinforcement in concrete. Lausanne: Fib; 2000.
28. Clark AP. Comparative bond efficiency of deformed concrete reinforcing bars. ACI Journal. 1946;37(6):399-407.
29. Angst UM, Geiker MR, Michel A, Gehlen C, Wong H, Isgor OB, et al. The steel–concrete interface. Mater Struct Constr. 2017;50(2):143.
30. Chang X, Chen Y, Lin H, Zhang Y. Modeling of fiber pullout behaviors of stiff fiber reinforced cementitious composites. Comput Concr. 2012;9(3):171-8.
31. Nematzadeh M, Ghadami J. Evaluation of interfacial shear stress in active steel tube-confined concrete columns. Comput Concr. 2017;20(4):469-81.
32. Rahdar HA, Ghalehnovi M. Post-cracking behavior of UHPC on the concrete members reinforced by steel rebar. Comput Concr. 2016;18(1):139-54.
33. Dai J, Harries KA, Yokota H. A critical steel yielding length model for predicting intermediate crack-induced debonding in FRP -strengthened RC members. Steel Compos Struct. 2008;8(6):457-73.
34. Kwak HG, Kim SP. Bond-slip behavior under monotonic uniaxial loads. Eng Struct. 2001;23(3):298-309.
35. ASTM: American Society for Testing and Materials. ASTM C1018: standard test method for flexural toughness and first-crack strength of fiber-reinforced concrete (using beam with third-point loading). West Conshohocken: ASTM; 1991.
36. Carmona JR, Ruiz G, del Viso JR. Mixed-mode crack propagation through reinforced concrete. Eng Fract Mech. 2007;74(17):2788-809.
37. Kotsovou GM, Kotsovos GM. Behaviour of RC Beams with non-bonded flexural reinforcement: a numerical experiment. Comput Concr. 2016;18(2):165-78.